Lewis acid–dominated aqueous electrolyte acting as co-catalyst and overcoming N₂ activation issues on catalyst surface

Ashmita Biswas[a,1] , Samadhan Kapse[b,1] , Bikram Ghosh[a], Ranjit Thapa[b] , and Ramendra Sundar Dey[a,2]

The growing demands for ammonia in agriculture and transportation fuel stimulate researchers to develop sustainable electrochemical methods to synthesize ammonia ambiently, to get past the energy-intensive Haber-Bosch process. However, the conventionally used aqueous electrolytes limit N_2 solubility, leading to insufficient reactant molecules in the vicinity of the catalyst during electrochemical nitrogen reduction reaction (NRR). This hampers the yield and production rate of ammonia, irrespective of how efficient the catalyst is. Herein, we introduce an aqueous electrolyte ($NaBF_4$), which not only acts as an N_2-carrier in the medium but also works as a full-fledged "co-catalyst" along with our active material MnN_4 to deliver a high yield of NH_3 (328.59 $\mu g\ h^{-1}\ mg_{cat}^{-1}$) at 0.0 V versus reversible hydrogen electrode. BF_3-induced charge polarization shifts the metal d-band center of the MnN_4 unit close to the Fermi level, inviting N_2 adsorption facilely. The Lewis acidity of the free BF_3 molecules further propagates their importance in polarizing the $N{\equiv}N$ bond of the adsorbed N_2 and its first protonation. This push-pull kind of electronic interaction has been confirmed from the change in d-band center values of the MnN_4 site as well as charge density distribution over our active model units, which turned out to be effective enough to lower the energy barrier of the potential determining steps of NRR. Consequently, a high production rate of NH_3 (2.45×10^{-9} mol s^{-1} cm^{-2}) was achieved, approaching the industrial scale where the source of NH_3 was thoroughly studied and confirmed to be chiefly from the electrochemical reduction of the purged N_2 gas.

$NaBF_4$ aqueous electrolyte | Lewis acid base adduct | d-band center | electrochemical nitrogen reduction reaction | industrial-scale ammonia production

Ammonia is considered the most abundant and widely used synthetic fertilizer in the world. The sole mean of large-scale ammonia production relies on the century-old Haber-Bosch process, which takes in more energy than it can produce, while the electrochemical nitrogen reduction reaction (NRR) offers a carbon-free and sustainable way of ammonia synthesis (1–4). However, electrochemical NH_3 synthesis is often arrested by a few factors, such as NH_3 detection, contaminations from source gases, nitrogen-containing chemicals, and the presence of labile nitrogen in the catalysts. In the recent past, several protocols have been proposed to correct the fallacious results (5, 6). Recently, Choi et el. concluded that it is difficult to believe from the too-low yield rate of NH_3 that the reduction of N_2 has actually occurred in the aqueous medium (6). However, to overcome this issue, several strategies include the material selectivity allowing selective N_2 adsorption rather than proton adsorption, production of sole product NH_3 rather than N_2H_4, one of the stable intermediates of NRR, and facile desorption of the end product (NH_3). Besides this, it is noteworthy that the electrolyte plays a crucial role and offers a suitable environment for any electrochemical reactions to occur. However, the issue with the solubility of N_2 in conventional aqueous electrolytes is a real hindrance to achieving a high yield and production rate of NH_3 during electrochemical synthesis. Therefore, it is necessary to solve the most important issue, that is, to solvate a promising concentration of N_2 molecules into the electrolyte such that it becomes accessible to the catalyst surface for its subsequent reduction.

A recent study by Ren et al. has elaborated that about 90.7% of the research works related to NRR have focused on the suitable catalyst development, while only 4.7% have been devoted to work on the electrolytes, which is indeed a very crucial factor for NRR, but is mostly overlooked and in infancy (7). In order to do away with the competitive hydrogen evolution reaction (HER), several researchers have sought the help of organic-based or molten hydroxide electrolytes that would lower the proton content in the electrolyte medium. Nonetheless, most organic electrolytes become unstable in the reducing environment of the catholyte, and the requirement of large amounts of organic solvents deviates from the goal of green NH_3 synthesis (8–12). Tsuneto et al. tried to further increase the NH_3 formation efficiency by incorporating Li^+ into the

Significance

The electrochemical ammonia synthesis is majorly limited by the poor solubility of N_2 in the aqueous electrolyte environment, besides the competitive hydrogen evolution reaction. In an attempt to solve these issues, the "ambient" conditions are mostly overlooked. This work is an approach to examine the long-standing issues about the solubility of N_2 in aqueous medium and achievement of industrial-scale production rate of ammonia by nitrogen reduction reaction (NRR) at ambient condition. Mechanistic investigation shows that Lewis acid (BF_3) has the capability to hold N_2 by forming a Lewis acid-base adduct, which further adsorbs on catalyst surface by a push-pull electronic effect. Therefore, this report may open new vistas to studying and understanding the role of the NRR in aqueous medium.

organic electrolyte (13). However, that is not a universal approach, as few metals have a tendency to form alloy with Li, thereby passivating it (14). Contrary to this, a special candidature has been given to the ionic liquids that serve as excellent nonaqueous electrolytes (15–18). Although several works have demonstrated the importance of fluorinated ionic liquids in solvating N_2 (19, 20), none of them offer a mechanistic investigation of the actual interaction role of ionic liquid. Moreover, it has been observed that ionic liquids help to elevate the Faradaic efficiency (FE) of NRR, but have very little impact on the yield and production rate of NH_3 (21). In fact, one of the serious limitations of the use of ionic liquids is that its high cost makes it unsuitable for commercial-scale use.

However, this does not in any way disregard the advantages of aqueous electrolytes because of their simplicity, economical friendliness, and proton exposure and transfer efficiency, which is again essential for the protonation steps of NRR. N_2 solubility is one of the major concerns of the aqueous electrolytes, where the electrolytes only serve as a platform for the NRR process to occur. Herein, we postulate a strategy in which $NaBF_4$ in water is taken as working electrolyte such that the electrolyte itself can act as a "co-catalyst" along with the active material to bring about a negotiable N_2 solubility and activation during NRR in ambient condition. We have thoroughly demonstrated the "bi-catalytic" activity of our electrode-electrolyte system reinforcing a high production rate for NH_3 synthesis. Nuclear magnetic resonance (NMR) studies reveal the existence of both BF_4^- and BF_3 in the medium. BF_3, having moderate Lewis acidity, forms an adduct with N_2 promoting its solubility in aqueous electrolyte. In this study, Mn-N/C with MnN_4 active unit has been chosen as a model catalyst, as N_2 is known to chemisorb on the transition metal by transferring an electron from its bonding orbital and accepting electron in its π^* antibonding orbital, which is requisite for the $N\equiv N$ bond activation (22–25). More interestingly, free BF_3 has been found to interact with both the catalyst active site (MnN_4) and the adsorbed N_2 molecules, where in the former, it helps in bond relocation by shifting the metal d-band center, and later in its activation, bond polarizability and first protonation at a detrimentally faster rate by a "push-pull" mechanism (25, 26). This manyfold influence of BF_3 on the electrode-N_2 system appears to be promising for the high yield of ammonia with a very good production rate, approaching the industrial-scale periphery (14).

Results

Conventional Electrolytes versus $NaBF_4$. Resolving the existing hurdle of N_2 activation in aqueous electrolytes was our prime focus in this study. Mostly, with the conventional aqueous electrolytes, the research focuses on the discussion of pH effect and the size of cations in suppressing HER, promoting NRR kinetics. While investigating a series of aqueous electrolytes, we determined that the anionic counterparts like Cl^-, OH^-, SO_4^{2-}, ClO_4^- can somewhat influence the catalyst active site for N_2 adsorption, but typically, these electrolytes have no interaction with N_2. Therefore, these do not serve as the role of "carrier" of N_2 into the medium, in vicinity of the catalyst, unlike $NaBF_4$ (27, 28). $NaBF_4$ in aqueous medium is easily hydrolyzed to form fluoroboric acid (HBF_4), which is considered as superacid with Hammett acidity function of -16.6 (29). The superacid HBF_4 exists in equilibrium between $H_3O^+ + [BF_4]^- \leftrightarrow H_2O.BF_3$ in aqueous medium. BF_3, being in the limelight of this work, has a multitudinous effect, not only on the catalyst (MnN_4) surface but also with N_2 as follows:

(a) Importantly, the tendency of interaction between the BF_3 and N_2 to form $N_2 \rightarrow BF_3$ adduct enables N_2 sufficiency in the three-phase interface (gas-liquid-solid) and in the proximity of the catalyst, which was so far a missing link for all other aqueous electrolytes.

(b) BF_3, on the other hand, imparts negative charge density from its nonbonding orbitals to the lowest unoccupied molecular orbital of MnN_4 (D_{4h} point group symmetry), as confirmed from the low negative metal d-band center value, close to Fermi level in presence of BF_3.

(c) The charge-polarized Mn center triggers the adsorption of N_2 molecules, and through σ-bonding and π-back bonding, interactions help in protonation of N_2.

(d) This N_2 activation and protonation step is further provoked by the Lewis acidic effect, served by free BF_3 (unlike all other anions) on the adsorbed N_2 molecules. The boron center of BF_3 pulls the electron density from the adsorbed N_2 and delocalizes the charge over terminal F atoms. The symbiotic electronic push-pull effect of BF_3-induced-$MnN_4 \rightarrow N_2$ and $N_2 \rightarrow$ free BF_3 leads to significantly improved N_2 activation, polarization, as well as first protonation on the catalyst surface in $NaBF_4$-rich aqueous electrolyte (26).

(e) Finally, the easy desorption of the final product NH_3, because of its increased solubility and interaction with BF_3, forms a frustrated Lewis acid base pair ($H_3N \rightarrow BF_3$).

The superiority of BF_3 compared with all other conventional aqueous electrolytes is schematically demonstrated in Fig. 1 *A–C*.

Promoting N_2 Solubility by the Lewis Acidic Effect of BF_3 in Aqueous Electrolyte. Our choice of electrolyte was such that (a) it would be a cheap, abundant, and water-soluble inorganic salt; and (b) it would deliver BF_3 in the medium for the plausible interaction with the purged N_2 gas. The existence of BF_3 in the aqueous solution of $NaBF_4$ was rightly confirmed from the NMR spectra of ^{11}B and ^{19}F (*SI Appendix*) (30, 31). BF_3 is known to have moderate Lewis acidity compared with other boron halides, because of the $p\pi$-$p\pi$ back bonding between the symmetry-matched 2p orbitals of F and B caused by a partial positive charge dominating over F, while the B center remains somewhat electronically sound. In the advent of any Lewis base, BF_4^- will have a tendency to exist as BF_3 and capture electron density to neutralize the partial positive charge over F. As an opportunity to this, in presence of N_2, not only BF_4^- will form $N_2 \rightarrow BF_3$ adduct but the N_2 may partly replace H_2O molecules from the $BF_3.H_2O$ to form $BF_3.N_2$, as can be seen from the higher field chemical shift of the peaks in the ^{11}B and ^{19}F NMR spectra (Fig. 2 *A* and *B*). A high field shift of 0.01 ppm and 0.08 ppm could be seen in the ^{19}F and ^{11}B NMR for the respective $BF_3.H_2O$ signals, which indicates a considerable gain of electronic charge on BF_3 that is delocalized from boron to fluorine. Unlikely, in the ^{19}F NMR, a greater high field shift of 0.12 ppm was seen for the peaks corresponding to $BF_3.DMSO$-d^6, presumably because N_2 serves as a better base and can replace DMSO-d^6 in the adduct. The signal corresponding to BF_4^- in the ^{11}B NMR displayed no change, as it is coordinatively and electronically already saturated. This interaction between N_2 and BF_3 could be supported by the rising ultraviolet (UV) peak at 265 nm when $NaBF_4$ solution was made to interact with N_2 for increasing feeding time (*SI Appendix*, Fig. S1). Simultaneously, by performing Hirshfeld surface analysis (*SI Appendix*, Fig. S2), the small effect of BF_3 on free N_2 molecules is clarified, which induces N_2 solubility in the electrolyte through weak Van der Waals interactive forces. This interaction induces N_2 solubility in the aqueous
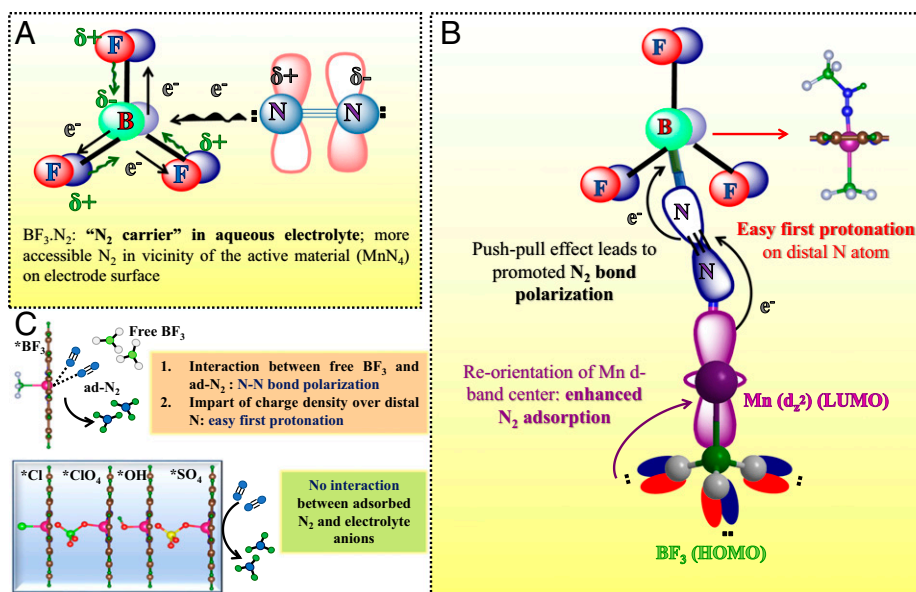
Fig. 1. (*A*) Role of BF$_3$ on free N$_2$ forming BF$_3$.N$_2$ adduct; N$_2$ solubility in aqueous medium. (*B*) BF$_3$ as a co-catalyst along with Mn-N$_4$ active site toward enhanced N≡N bond activation, polarization, and first protonation. (*C*) Advantages of BF$_3$ as an anion, compared with the other conventional electrolytes (anions like Cl$^-$, ClO$_4^-$, OH$^-$, SO$_4^{2-}$). HOMO, highest occupied molecular orbital; LUMO, lowest unoccupied molecular orbital.

medium, where BF$_3$ typically acts as a "sink" for N$_2$, as schematically shown in Fig. 2*C*, and enhances N$_2$ accessibility in the vicinity of the active material, which was so far a distant dream with any of the conventional electrolytes in practice.

Structural Evidence and Characterization of the Catalyst. Due to the proper energy and symmetry of the metal 3d orbital enabling N$_2$ activation, Mn embedded in an *N*-doped carbon matrix is taken into account as a model system for our
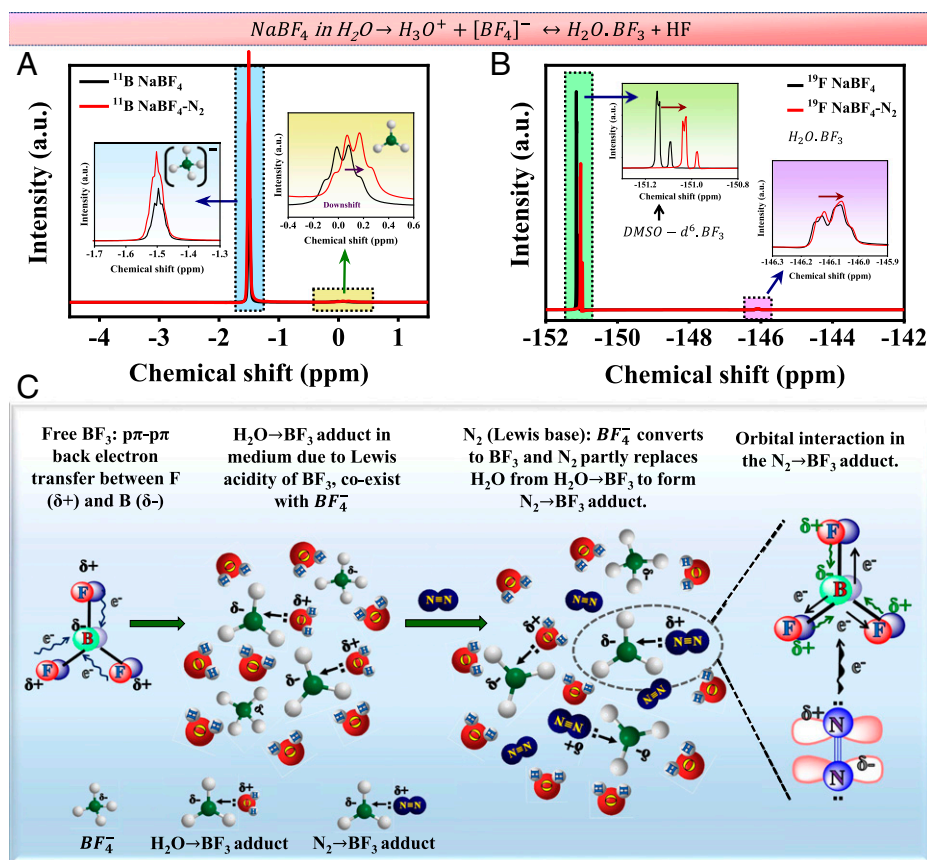

Fig. 2. (*A*) ^{11}B-NMR spectra of NaBF$_4$ in DMSO-d^6 in ambient and N$_2$ purged conditions. *Inset* represents the quartet and skewed multiplet peaks for B-F coupling representing coexistence of BF$_3$.H$_2$O and BF$_4^-$ in the medium. (*B*) ^{19}F-NMR spectra of NaBF$_4$ in DMSO-d^6 in ambient and N$_2$ purged conditions. *Inset* represents the skewed quartet signal coming from ^{10}BF$_3$.H$_2$O and ^{11}BF$_3$.H$_2$O due to F-H coupling and singlet peaks for F representing BF$_3$.DMSO-d^6 in the medium. (*C*) Schematic representation of the interaction between BF$_3$ and N$_2$ forming N$_2$→BF$_3$ adduct.
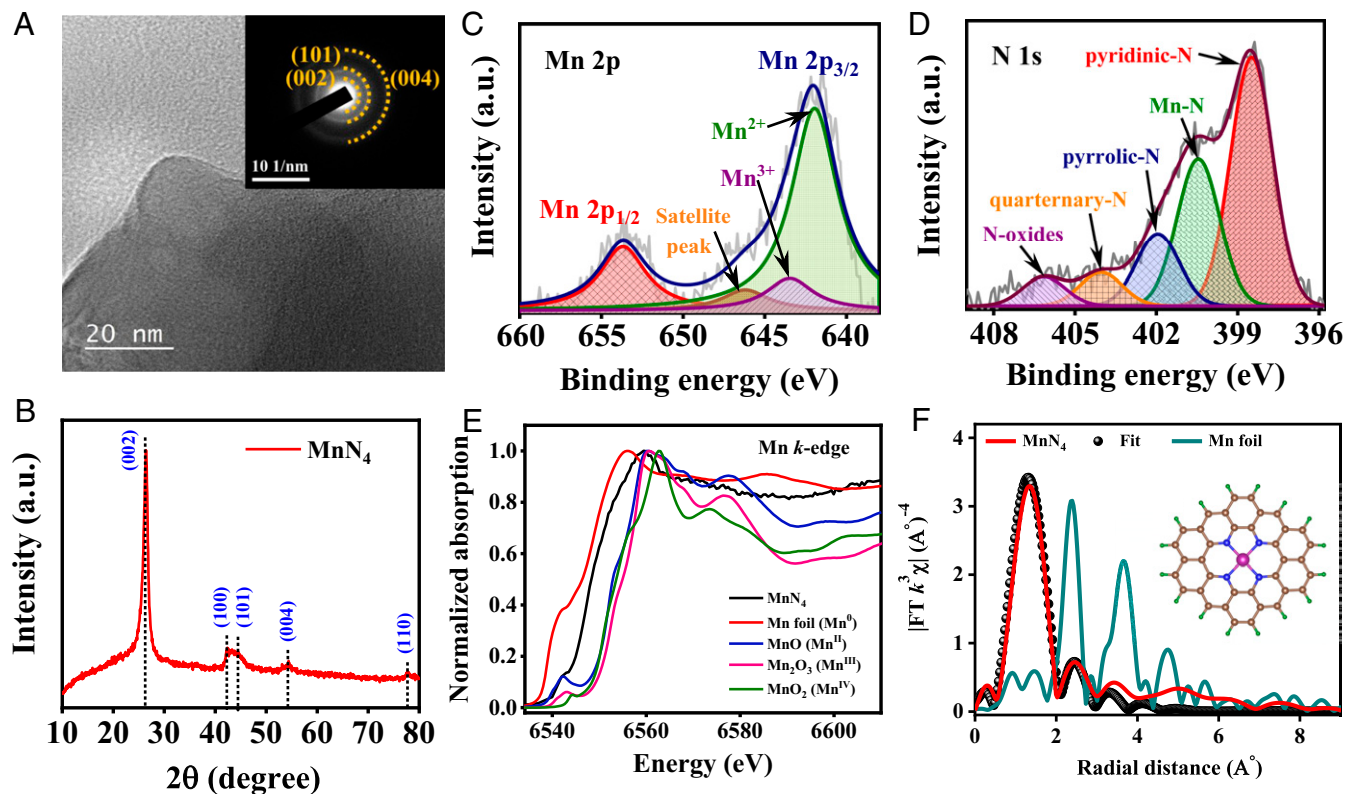
Fig. 3. (*A*) High-resolution transmission electron microscopy image for the as-obtained MnN$_4$. *Inset* shows the exposed surfaces of {002}, {101}, and {004} in the SAED (selected area electron diffraction) pattern (scale bars: 20 nm) (*A*) and 10 1/nm (*Inset*). (*B*) XRD patterns for MnN$_4$ denoting the diffraction peak for carbon. (*C*) Deconvoluted XPS profile for the Mn 2p of MnN$_4$ catalyst indicating spin-orbit coupled peaks at an 11.67 eV separation. (*D*) Deconvoluted XPS profile for the N 1s spectra for MnN$_4$ catalyst. (*E*) Normalized X-ray absorption near-edge spectroscopy spectra at the Mn *k*-edge of Mn foil, MnO, Mn$_2$O$_3$, MnO$_2$, and MnN$_4$. (*F*) Fourier-transform extended X-ray absorption fine structure (FT-EXAFS) spectra of Mn foil and MnN$_4$, and the curve fitting with the Mn−N1. The *Inset* represents the corresponding atomic model.

investigating catalyst (32). The catalyst synthesis involves simple mechanical grinding followed by carbonization at 800 °C with a slow reaction rate of 3 °C min^{-1} to obtain our final material MnN$_4$ (details are provided in the experimental section). A sheet-like morphology could be observed in the image (Fig. 3*A*), and the corresponding selected area electron diffraction (SAED) pattern displays the dominant (002), (101), and (004) surfaces of carbon (Fig. 3 *A*, *Inset*). X-ray diffraction (XRD) analysis suggests that the catalyst is crystalized in the hexagonal carbon phase (space group P63/mmc) (*SI Appendix*, Table S1). The planes obtained from SAED are quite consistent with those obtained from XRD data in Fig. 3*B*. The sp^2 hybridized carbon plane with defects caused by N and Mn dopants was verified from the Raman spectra with an I_D/I_G ratio of 0.94, where the ratio of the peak intensities of D-band (I_D) to that of G-band (I_G) denotes the extent of disorderness prevalent in the material, with a precise 2D peak indicating the formation of few-layered Mn and N codoped all planar-graphene sheet (*SI Appendix*, Fig. S3). The formation of Mn-N bond was confirmed from the Mn-N stretching vibration at ∼614 cm^{-1} in the Fourier transform (FT) infrared spectrum (*SI Appendix*, Fig. S4) (33). The valency of the Mn atom was shown from the X-ray photoelectron spectroscopy (XPS) analysis, where the high-resolution deconvoluted Mn spectra displayed distinct spin-orbit coupled Mn 2p peaks with a doublet separation of 11.67 eV (Fig. 3*C*) (34). The deconvoluted N 1s spectra displayed peaks corresponding to pyridinic N, pyrrolic N, quaternary N, *N*-oxides, and Mn-N$_x$ peaks with 30.8%, 19.72%, 13.51%, 8.59%, and 27.38%, respectively (Fig. 3*D* and *SI Appendix*, Table S2A). Further details about XPS are elaborated

in *SI Appendix*, Fig. S5. The atomic percent of all the elements from XPS analysis is presented in *SI Appendix*, Table S2B, which was congruent with what we obtained from energy dispersive X-ray analysis (*SI Appendix*, Fig. S6 and Table S3). The X-ray absorption near-edge spectroscopy profile demonstrated that the active species Mn exhibited an oxidation state in between 0 and +3 (Fig. 3*E*). The FT k^3-weighted extended X-ray absorption fine structure (EXAFS) spectra in Fig. 3*F* showed that, for MnN$_4$, only a primary peak at 1.76 Å can be observed, without the signal of the Mn−Mn shell (compared with Mn foil), which further proves that there was no agglomeration of Mn atoms in the form of nanoparticles, in agreement with XRD. EXAFS shell-fitting analysis in *SI Appendix*, Table S4, indicated four *N*-coordinate Mn centers (MnN$_4$) in MnN$_4$ catalyst (32). The electrochemical active surface area of the material MnN$_4$ (Anecsa) was calculated to be 0.108 cm^2 on the glass carbon electrode using Eq. **S1** in *SI Appendix* (*SI Appendix*, Fig. S7) (35). The N-doped carbon (N-C) control sample was synthesized without the metal precursor (*SI Appendix*) for a comparative study to exaggerate the role of the metal center in presence of the electrolyte anions for the noteworthy NRR performance. The XRD spectra of the control sample resembles that of the graphitic carbon with predominant peaks at 26° and 42°, as shown in *SI Appendix*, Fig. S8.

Effect of Surface-Adsorbed BF$_3$ on the In Situ Electrochemical Conversion of N$_2$ to NH$_3$. The key factor to improve the production rate of ammonia is by improving the kinetics of the potential determining steps (PDS) of NRR. In general, the probable rate-determining steps are: (a) N$_2$ adsorption, owing to the poor

accessibility and interaction of N_2 onto the catalyst surface; (b) first protonation, because of the polarizability issue of N_2 and high-energy-intensive proton affinity of N_2 (493.8 kJ mol^{-1}) (36); and (c) desorption of the target product (NH_3). Among these, for MnN_4 type of systems, it has been theoretically proved that the first protonation of N_2 is the potential limiting step (37). With the BF_3-dominated aqueous electrolyte, it was possible to effectively overcome all these issues and bring about a low overpotential for NRR with a high production rate. The electrochemical response of NRR activities of the catalyst was primarily obtained from the linear sweep voltammetry curves for $NaBF_4$-N_2 system, which differed in current density from the Ar-saturated electrolyte condition. It is to be noted that all potential values mentioned in this work are calibrated with respect to reversible hydrogen electrode (RHE), following *SI Appendix*, Eq. **S2**. Interestingly, the $NaBF_4$-catalyst system also outperformed all the conventional electrolytes, like HCl, Na_2SO_4, $LiClO_4$, and KOH, in terms of both onset potential and current densities (*SI Appendix*, Fig. S9 and Table S5). To no surprise, extensive potential-dependent studies and corresponding UV-visible (UV-vis) spectra (*SI Appendix*, Figs. S10–S14) revealed that the production rate, yield, and FE for NH_3 formation was exceedingly high in the case of 0.5 M $NaBF_4$ than all other electrolytes, owing to the minimum free energy requirement of the catalyst in $NaBF_4$ for the first protonation of adsorbed N_2, as shown in Fig. 4 *A* and *B*. In all cases, the concentration of NH_3 and N_2H_4 (side product) was calculated from the UV-vis calibration curves obtained from the respective indophenol-blue and Watt and Chrisp methods (*SI Appendix*, Figs. S15–S17); details are discussed in the experimental section in *SI Appendix*. The maximum yield for NH_3 in 0.5 M $NaBF_4$ was obtained at 0 V versus RHE (328.59 µg h^{-1} mg$_{cat}^{-1}$), with an FE of 18.6% (*SI Appendix, Eqs.* **S3** *and* **S4**). This exceedingly high yield of NH_3 could also be attributed to the product specificity of our catalyst during NRR, as there was no evidence of the side product (N_2H_4) formation (*SI Appendix*, Fig. S18).

A vivid theoretical study was carried out with the five different types of anions for respective electrolytes, such as BF_3 ($NaBF_4$), Cl (HCl), ClO_4 ($LiClO_4$), OH (KOH), and SO_4 (Na_2SO_4) (*SI Appendix*, Fig. S19) to gain insight about the solvation effect. By considering each anion attached with the Mn site, we calculated the free energy profile of N_2 and NNH (the first protonated N2 and the potential determining intermediate of NRR) adsorption (*SI Appendix*, Fig. S20). We observed ΔG_{N2} in the following order: -0.59 eV (BF_3) < -0.53 eV (Cl) < -0.22 eV (ClO_4) < -0.1 eV (OH) < 0.11 eV (SO_4). The BF_3 anion showed the higher N_2 adsorption for NRR, and the trend was matching with the experimental study. The corresponding values of overpotential (η) were 0.54, 0.75, 1.01, 0.95, and 1.08 V respectively. Whereas these electrolytes (except BF_3 anion) did not play a role in the N_2 polarization, where the structural distortion was observed after attaching these anions to the adsorbed N_2. For more clarity, we computed the d-band center values of Mn site attached with different electrolyte anions (BF_3, Cl, ClO_4, OH, SO_4). From this investigation, a linear relationship was observed between d-band center shift and the adsorption of N_2, as well as NNH intermediate on the Mn site (*SI Appendix*, Fig. S21). The Mn site with attached BF_3 shows (-1.55 eV) the highest d-band center (lower negative value) that is the origin of its higher NNH adsorption and lower thermodynamic overpotential of NRR. Therefore, the electrolyte with BF_3 anion is the most promising medium for strong N_2 adsorption, low NRR overpotential, and N_2 polarization to synthesize NH_3 with high yield rate. To exaggerate the role of BF_3 on MnN_4 active site,

the control sample *N*-C was also subjected to chronoamperometry at 0.0 V (*SI Appendix*, Fig. S22A), only to find the NH_3 yield to be 80.34 µg h^{-1} mg$_c^{-1}$, which is much lower compared with Mn/*N*-C material. The FE was also as low as 5.9% (*SI Appendix*, Fig. S22 *B and C*). This was expected, as BF_3 played a major role on the Mn active site in altering the metal d-band center, which in turn helped in facile N_2 adsorption and its subsequent reduction. The result was absolutely in congruence with the electrochemical impedance studies of MnN_4 catalyst in different electrolyte conditions, where the minimum ohmic and charge-transfer resistance could be evident in the MnN_4-$NaBF_4$ interface (*SI Appendix*, Fig. S23). The NRR performance of our active system and all the electrolytes are tabulated in *SI Appendix*, Tables S6 and S7.

For five consecutive NRR cycles at 0 V (2 h each) with the same electrode (*SI Appendix*, Fig. S24A), the NRR performance remained in harmony with respect to the yield, FE, and area-normalized production rate of NH_3, as evident from *SI Appendix*, Fig. S24 *B–D*. The negligible deterioration in performance could be put upon to the insignificant mass loss from the electrode surface upon prolonged exposure to the reaction conditions. The BF_3-N_2-MnN_4 interaction could be further established from the increasing NH_3 concentration in the catholyte upon increasing the potential-dependent experiment time from 2 h to 4h to 8h (*SI Appendix*, Fig. S25A), as evident from the from the ^{1}H-NMR data for $^{14}NH_3$ and the UV-vis spectra in Fig. 4 *C* and *SI Appendix*, Fig. S25 *B*, respectively.

In order to verify the reliability of the produced NH_3 from the feeding gas, it was necessary to ensure that there were no contaminants, either in the feed gas, electrolyte, or from the cathode material. A measurement as low as 0.01 µmol of *N*-impurity was estimated in the $^{14}N_2$ feeding gas (*SI Appendix*, Table S8), which was thoroughly avoided by passing it through acid and base traps to obtain the pure gas as found from gas chromatography and UV-vis spectroscopic measurements (*SI Appendix*, Figs. S26-S28), used for all the electrochemical measurements. From the standard curve for NO_x in *SI Appendix*, Fig. S29 *A and B*, and the corresponding UV-vis spectra of all the bare electrolytes at ~540 nm, it was verified that there was no NO_x contamination in the medium. Most importantly, the isotope labeling experiment with $^{15}N_2$ feeding gas was performed in 0.5 M $NaBF_4$ at 0 V, as shown in *SI Appendix*, Fig. S30. While the ^{1}H NMR spectrum corresponding to $^{14}NH_3$ displayed a triplet coupling with a J_{N-H} of 52 Hz (38), a doublet coupling with nonidentical peak positions was observed for the $^{15}NH_3$ with a J_{N-H} of 72 Hz, and there was no NMR signal for the Ar purged experiment and under no potential in the $^{14}N_2$-MnN_4-BF_3 system (Fig. 4*D*). In order to further ensure the purity of the NH_3 produced, vigorous comparative quantifications are essential with both the $^{14}N_2$ and $^{15}N_2$ gases via colorimetric and NMR methods (details are provided in *SI Appendix*; S*I Appendix, Eq.* **S5**; and *SI Appendix*, Fig. S31). According to our observation, the calculated yield of NH_3 and the mass-normalized production rate from $^{15}N_2$ gas accords well with that obtained from $^{14}N_2$ gas (Fig. 4*E*), which further confirms that the NH_3 was chiefly produced by electroreduction of N_2 on the Mn-N_4 catalyst surface with the help of BF_3. A broad literature survey reveals that our electrode-electrolyte system in ambient aqueous condition is considerably better than the ionic liquid, conventional aqueous, and also aqueous/organic electrolytes, and is nearly comparable with the Li-mediated approach of NH_3 synthesis in terms of NH_3 yield and area-normalized production rate as summarized in Fig. 4*F*. Furthermore, negligible NH_3 formation
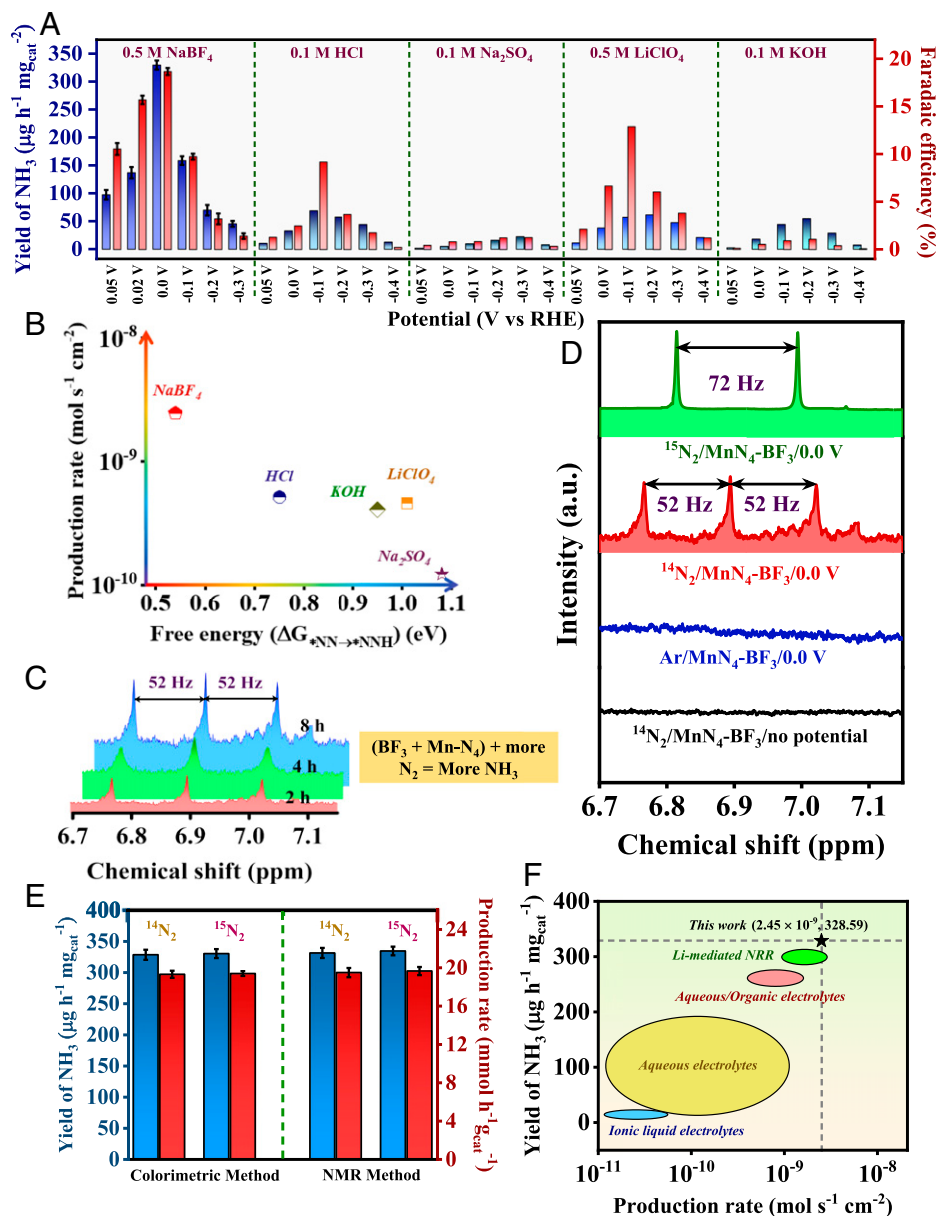
Fig. 4. (*A*) Comparison of yield of NH$_3$ and corresponding Faradaic efficiency for MnN$_4$ catalyst in different electrolytes at different potentials. The trend for all the activity descriptors follows NaBF$_4$ > HCl > LiClO$_4$ > KOH > Na$_2$SO$_4$. (*B*) Comparison plot of free energy change for the first protonation step versus production rate of NH$_3$ for MnN$_4$ catalyst in different electrolyte conditions. (*C*) ^{1}H-NMR spectra of the working electrolyte in DMSO-d^6 after different time span of the potential-dependent experiment at 0 V versus RHE. (*D*) Isotope labeling experiment in 400 MHz NMR spectrophotometer; ^{1}H NMR spectra obtained after electrolysis in 0.5 M NaBF$_4$ with ^{15}N$_2$, ^{14}N$_2$, and Ar as the feeding gases. (*E*) Comparison of ammonia yield and mass-normalized production rate quantified by both colorimetric test and NMR measurement with ^{14}N$_2$ and ^{15}N$_2$ feeding gases. The error bars in (*A*) and (*E*) represent the SD between identical electrolysis experiments. (*F*) NRR performance map on the basis of area-normalized production rate and mass-normalized yield of NH$_3$ in traditional aqueous, aqueous/organic, ionic liquid electrolytes, and Li-mediated NRR over current state-of-the-art electrocatalysts.

in the blank experiments in (a) Ar purged condition and (b) at open circuit potential under N$_2$ ensured that there was no participation of the catalyst-N in the high yield of NH$_3$ (*SI Appendix,* Fig. S32).

Thermodynamics of BF$_3$-Induced NRR in Terms of d-Band Center of Metal and Origin of the Activity toward NRR. We performed Density Functional Theory (DFT)-based calculations to understand the NRR mechanism, effect of electrolyte, and origin of catalytic performance in MnN$_4$ catalyst. We considered four energy-optimized model systems, like pristine MnN$_4$, MnN$_4$ attached to BF$_3$ (MnN$_4$/BF$_3$), MnN$_4$ in presence of free BF$_3$ anion (MnN$_4$ (BF$_3$)), and MnN$_4$ attached to BF$_3$ in presence of free BF$_3$ anion (MnN$_4$/BF$_3$ (BF$_3$)) (*SI Appendix,* Fig. S33). For these four models, the NRR

mechanism and the full free energy profile (*SI Appendix,* Fig. S34 and Fig. 5*A*) inferred that the alternating pathway is preferred over the distal pathway due to the lower value of free energy change of the NHNH step compared with the NNH$_2$ step (39–41), whereas the enzymatic or mixed mechanism is not feasible on MnN$_4$ systems due to the higher value of change in Gibbs free energy of N$_2$ adsorption (ΔG$_{N2}$) with end-on configuration (–0.38 eV) than that of side-on configuration (–0.066 eV).

We extrapolated our finding to the free energy profile of N$_2$ and NNH adsorption to compare the NRR performance vividly (Fig. 5*B*). The optimized structures of N$_2$ and NNH adsorbed systems with the bond lengths between the molecule and active sites are given in *SI Appendix,* Fig. S35. First, we compared the N$_2$ adsorption energies for the four models. The values of ΔG$_{N2}$ for MnN$_4$, MnN$_4$ (BF$_3$), MnN$_4$/BF$_3$, and
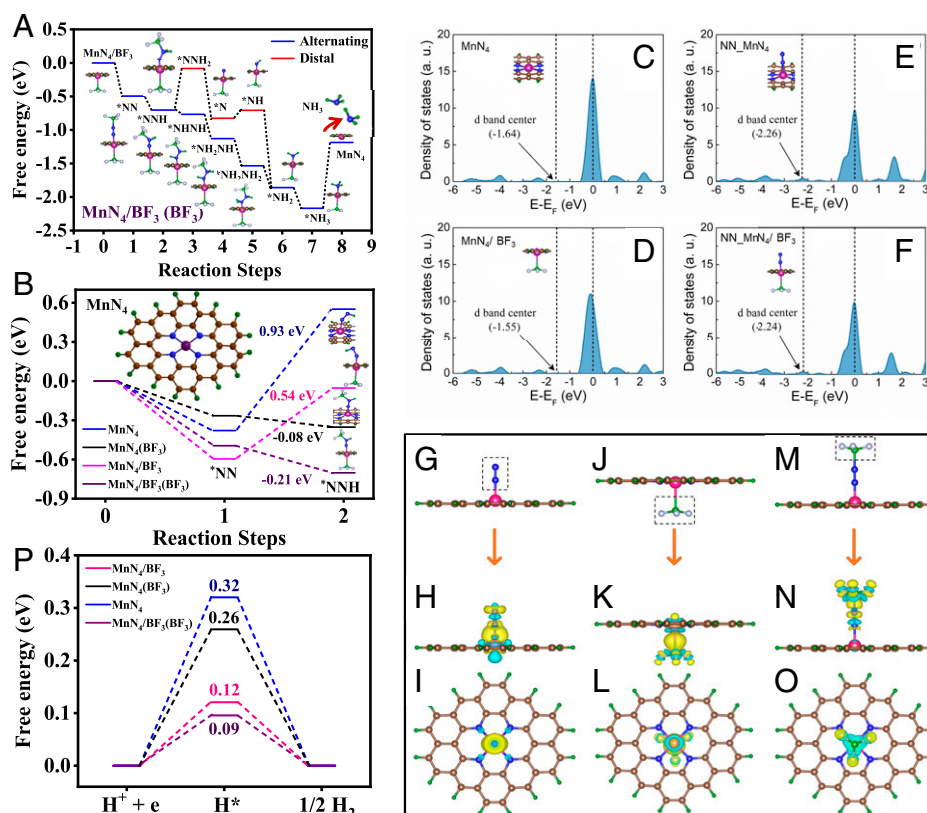
Fig. 5. Thermodynamic studies of NH$_3$ formation through BF$_3$-induced NRR on MnN$_4$ catalyst and electronic properties. (*A*) The full free energy path of NRR on the model system MnN$_4$/BF$_3$ (BF$_3$), being most energetically suitable for NRR. The full path illustrates the associative alternative pathway to be more favored over the distal pathway. (*B*) Free energy profile of N$_2$ and NNH adsorption for the four catalyst models, namely, pristine MnN$_4$, MnN$_4$ (BF$_3$), MnN$_4$/BF$_3$, and MnN$_4$/BF$_3$ (BF$_3$). The Mn, N, C, F, B, and H atoms are denoted with pink, dark blue, gray, light blue, big green sphere, and small green color sphere, respectively. (*C–F*) The d orbital density of states of Mn site in (*C*) pristine MnN$_4$, (*D*) MnN$_4$/BF$_3$, (*E*) N$_2$ adsorbed MnN$_4$, and (*F*) N$_2$ adsorbed MnN$_4$/BF$_3$. The d-band center value is given in the respective subfigure. Dotted line at zero in the x axis represents the Fermi energy level. (*G–O*) The optimized model structure, charge density difference with side view and top view of (*G–I*) N$_2$ adsorbed MnN$_4$, (*J–L*) MnN$_4$/BF$_3$, and (*M–O*) N$_2$ adsorbed MnN$_4$ with BF$_3$ attachment. The yellow and blue color lobes represent the charge accumulation and depletion with isosurface value of 0.0032 e/Å^3. (*P*) Represents the free energy diagram of HER for these four model systems with the value of ΔG$_H$.

MnN$_4$/BF$_3$ (BF$_3$) catalysts were –0.38, –0.26, –0.59, and –0.49 eV, respectively. We found that the nitrogen adsorption was exothermic (negative ΔG$_{N2}$) for all four models, and in particular, MnN$_4$/BF$_3$ showed higher N$_2$ adsorption among them, which could be attributed to the charge redistribution between BF$_3$ and MnN$_4$ imparting a local charge density over Mn active site. From the projected density of states study, the d-band center (ε_d) values (42) of Mn site in MnN$_4$ and MnN$_4$/BF$_3$ catalysts were –1.64 and –1.55 eV, respectively (Fig. 5 *C* and *D*). The higher ε_d value in MnN$_4$/BF$_3$ indicated that the binding of BF$_3$ anion influenced the chemistry of the Mn site by shifting the ε_d toward the Fermi level that led to the strong N$_2$ and NNH adsorption compared with pristine MnN$_4$ (43). Furthermore, the negative shift of ε_d (laying at –2.26 eV for MnN$_4$ and –2.24 eV for MnN$_4$/BF$_3$) was observed after N$_2$ adsorption, which revealed that the charge transfer occurred from the Mn site to N$_2$ during adsorption (Fig. 5 *E* and *F*). To visualize these charge transfers, we performed the charge density difference analysis. The charge redistribution was observed on the Mn site due to the attachment of both N$_2$ and BF$_3$ anion (Fig. 5 *G–L*) (BF$_3$ to MnN$_4$ to N$_2$). Second, the formation of the NNH intermediate during first protonation is the known PDS that defines the overpotential for NRR (η_{NRR}) (44). It was observed that the MnN$_4$ and MnN$_4$/BF$_3$ showed the overpotential of 0.93 and 0.54 V, respectively, whereas for systems MnN$_4$ (BF$_3$) and MnN$_4$/BF$_3$ (BF$_3$), the PDS step was exothermic in nature. Under the

N$_2$-adsorbed-MnN$_4$ condition, N$_2$ behaved as a better "base" to attract the free BF$_3$ ions in the medium and pass on the electronic charge to F through B center via a push-pull mechanism, which eventually helped to polarize N$_2$. Here, we examined negligible change in the ε_d value of the Mn center (–2.27 eV in NN_MnN$_4$ (BF$_3$) and –2.24 eV in NN_MnN$_4$/BF$_3$ (BF$_3$)) (*SI Appendix*, Fig. S36) that indicated there was no charge transfer found on Mn site, while charge redistribution was prevalent on N$_2$ (push-pull effect), which thereby boosted the first protonation process at the distal N for the initiation of NH$_3$ synthesis (Fig. 5 *M–O*). From the full free energy profile, we could find that the last step of NH$_3$ release for MnN$_4$/BF$_3$ (BF$_3$) system showed an energy barrier of 0.98 eV, but this step was not involved in the NRR mechanism due to high NH$_3$ solubility in the BF$_3$-dominated medium forming a frustrated Lewis pair as NH$_3$→BF$_3$ (45). We can infer that the overpotential can be exothermic and endothermic within a maximum value of 0.54 V in presence of BF$_3$ anion under its different binding positions. Overall, we can conclude that the binding or presence of BF$_3$ anion improves the N$_2$ adsorption and reduces the η_{NRR}.

Dominance of NRR over HER. HER is a well-known competitive pathway that hinders the production efficiency and NH$_3$ yield of NRR (46). For our model systems (*SI Appendix*, Fig. S37), we estimated that the values of change in Gibbs free energy of hydrogen adsorption (ΔG$_H$) for pristine MnN$_4$, MnN$_4$ (BF$_3$), MnN$_4$/BF$_3$, and MnN$_4$/BF$_3$ (BF$_3$) catalysts were +0.32, +0.26,

+0.12, and +0.09 eV, respectively (Fig. 5*P*). Importantly, we observed the endothermic nature of HER in all these models, which thereby favored the exothermic nitrogen adsorption (negative value of ΔG_{N2}) more ($\Delta G_{N2} < \Delta G_H$). Especially, the hydrogen poisoning effect (47) on Mn active site could be avoided due to the positive values of ΔG_H.

Approaching Industrial-Scale Production Rate of NH₃. The primary objective of this work was to overcome the rate-determining steps of NRR with an improvised aqueous electrolyte system (NaBF₄), which served as an ideal co-catalyst along with MnN₄. BF₃-induced overall charge polarization triggered the feasible N₂ reduction on the MnN₄ active site at a low overpotential with a successive high yield of NH₃ synthesis (328.59 µg h⁻¹ mg$_{cat}$⁻¹), which is so far the highest among all the conventional aqueous electrolyte-induced NRR, irrespective of the catalysts (Fig. 6*A* and *SI Appendix*, Table S9). Additionally, this work turned out to be tremendously beneficial in terms of the area-normalized production rate (*SI Appendix*, Eq. **S6**), as high as 2.45 × 10⁻⁹ mol s⁻¹ cm⁻², which almost approaches the industrial-scale periphery (14). However, one could be cautious of the catalyst with high area-normalized NH₃ production yet a low mass-normalized one. Thus, we also report the mass-normalized NH₃ production following *SI Appendix*, Eq. **S7**, which helped to evaluate and compare the NH₃ synthesis rate over wide-ranging approaches, electrolytes, and catalyst systems. In every respect, NaBF₄-MnN₄ catalyzed NRR (this work) functioned better than all the conventional systems being worked upon so far, as could be seen from the area as well as mass-normalized NH₃ production rate plot in Fig. 6*B* and *SI Appendix*, Table S10 (48).

Discussion

The widely highlighted problem of NRR that is the competitive HER is most likely worked upon with several catalyst development and electrolyte modifications, while the N₂ solubility and activation issues in the aqueous medium are generally neglected. This work justifies our aim to contribute toward this problem by using NaBF₄ as a working electrolyte, which served as a "full-packaged co-catalyst," along with MnN₄, reinforcing the NRR kinetics at the cost of low overpotential. The Lewis acidic nature of BF₃ induced adduct formation with the N₂ molecules and acted as a carrier of N₂ gas into the medium in the vicinity of the electrocatalyst. Simultaneously, the charge polarization over MnN₄ active site due to BF₃ delocalized the metal d-band center, which triggered N₂ adsorption on the catalyst site. Under this condition, free BF₃ form the medium interacted with the adsorbed N₂ and brought about the facile polarization of the N≡N bond and its first protonation at a much lower energy barrier. This push-pull charge-transfer effect enormously helped to overcome the PDS, and this BF₃-mediated NRR resulted in a huge production rate of NH₃, which could be compared to that on an industrial scale, which was not achieved so far with any aqueous or ionic liquid electrolytes.

In short, this kind of user-friendly aqueous electrolyte is being investigated for NRR. Since BF₃ displayed tremendous potential in triggering the kinetics of NRR, this finding may encourage researchers to work more on aqueous electrolyte designing toward an even better NRR performance of the
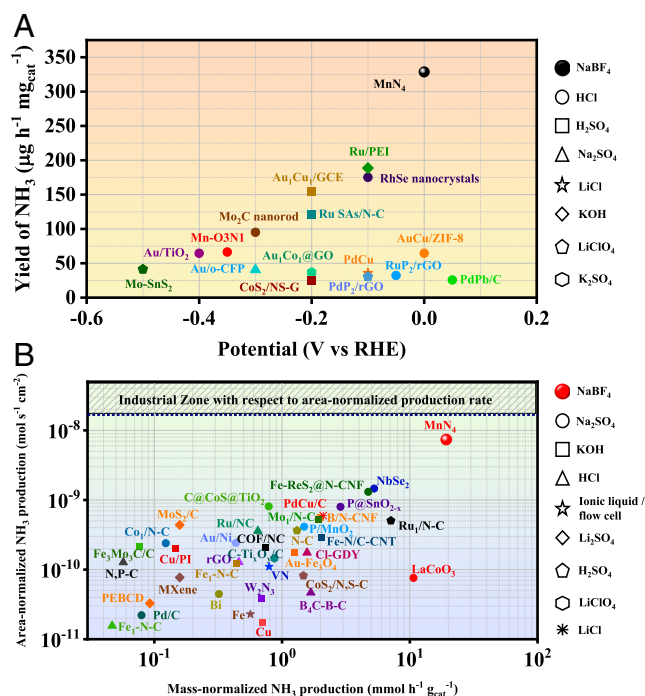

Fig. 6. (*A*) Yield of NH₃ in the potential range of −0.5 to 0.2 V versus RHE. (*B*) Area- and mass-normalized production rate of NH₃. The respective symbols adjacent to (*A*) and (*B*) denote the corresponding working electrolytes. Area-normalized production rate of NH₃ with MnN₄ in 0.5 M NaBF₄ (this work) was calculated to be 2.45 × 10⁻⁹ mol s⁻¹ cm⁻², approaching the predicted industrial-scale periphery. All the data included in both the figures are analyzed at ambient temperature and pressure.

electrocatalysts. In addition, electrocatalysts could also be functionalized with BF₃ derivatives, which could be one entirely new route of study in the field of NRR.

Materials and Methods

The synthetic strategy and experimental sections of this work are provided in *SI Appendix*. These methods contain the synthesis of Mn-N/C catalyst, structural characterizations. Detailed electrochemical measurements under ambient conditions are also included, along with N₂ gas purification details. The colorimetric methods for detection of ammonia, hydrazine, and NOₓ impurities; the calculation method for NH₃ yield, production rate, and FE; and the computation theory are elaborated in *SI Appendix*.

Data, Materials, and Software Availability. All study data are included in the article and/or supporting information.

1. G. Soloveichik, Electrochemical synthesis of ammonia as a potential alternative to the Haber–Bosch process. *Nat. Catal.* **2**, 377–380 (2019).
2. D. R. Macfarlane *et al.*, Perspective: A roadmap to the ammonia economy. *Joule* **4**, 1186–1205 (2020).
3. C. Liu, K. K. Sakimoto, B. C. Colón, P. A. Silver, D. G. Nocera, Ambient nitrogen reduction cycle using a hybrid inorganic-biological system. *Proc. Natl. Acad. Sci. U.S.A.* **114**, 6450–6455 (2017).
4. W. W. Weare *et al.*, Catalytic reduction of dinitrogen to ammonia at a single molybdenum center. *Proc. Natl. Acad. Sci. U.S.A.* **103**, 17099–17106 (2006).

5. L. Li, C. Tang, D. Yao, Y. Zheng, S. Qiao, Electrochemical nitrogen reduction: Identification and elimination of contamination in electrolyte. *ACS Energy Lett.* **4**, 2111–2116 (2019).

6. J. Choi *et al.*, Identification and elimination of false positives in electrochemical nitrogen reduction studies. *Nat. Commun.* **11**, 5546 (2020).

7. Y. Ren *et al.*, Strategies to suppress hydrogen evolution for highly selective electrocatalytic nitrogen reduction: Challenges and perspectives. *Energy Environ. Sci.* **14**, 1176–1193 (2021).

8. K. Kim *et al.*, Electrochemical reduction of nitrogen to ammonia in 2-propanol under ambient temperature and pressure. *J. Electrochem. Soc.* **163**, 610–612 (2016).

9. S. Chen *et al.*, Electrocatalytic synthesis of ammonia at room temperature and atmospheric pressure from water and nitrogen on a carbon-nanotube-based electrocatalyst. *Angew. Chem. Int. Ed. Engl.* **56**, 2699–2703 (2017).

10. D. Bao *et al.*, Electrochemical reduction of N_2 under ambient conditions for artificial n_2 fixation and renewable energy storage using N_2/NH_3 cycle. *Adv. Mater.* **29**, 1604799 (2017).

11. S. Licht *et al.*, Ammonia synthesis by N_2 and steam electrolysis in molten hydroxide suspensions of nanoscale Fe 2O3. *Science* **345**, 637 (2014).

12. Y. Ren *et al.*, Methanol-mediated electrosynthesis of ammonia. *ACS Energy Lett.* **6**, 3844–3850 (2021).

13. A. Tsuneto, A. Kudo, T. Sakata, Efficient electrochemical reduction of N_2 to NH_3 catalyzed by lithium. *Chem. Lett.* **22**, 851–854 (1993).

14. X. Zhao *et al.*, Comprehensive understanding of the thriving ambient electrochemical nitrogen reduction reaction. *Adv. Mater.* **33**, e2007650 (2021).

15. D. R. Macfarlane *et al.*, Ionic liquids and their solid-state analogues as materials for energy generation and storage. *Nat. Rev. Mater.* **1**, 15 (2016).

16. D. R. MacFarlane *et al.*, Energy applications of ionic liquids. *Energy Environ. Sci.* **7**, 232–250 (2014).

17. B. A. Rosen *et al.*, Ionic liquid-mediated selective conversion of CO_2 to CO at low overpotentials. *Science* **334**, 643–644 (2011).

18. G. R. Zhang, M. Munoz, B. J. M. Etzold, Accelerating oxygen-reduction catalysts through preventing poisoning with non-reactive species by using hydrophobic ionic liquids. *Angew. Chem. Int. Ed. Engl.* **55**, 2257–2261 (2016).

19. D. Almantariotis *et al.*, Influence of fluorination on the solubilities of carbon dioxide, ethane, and nitrogen in 1-n-fluoro-alkyl-3-methylimidazolium bis(n-fluoroalkylsulfonyl)amide ionic liquids. *J. Phys. Chem. B* **121**, 426–436 (2017).

20. C. S. M. Kang, X. Zhang, D. R. Macfarlane, Synthesis and physicochemical properties of fluorinated ionic liquids with high nitrogen gas solubility. *PhysChemComm* **122**, 24550–24558 (2018).

21. I. Harmanli, N. V. Tarakina, M. Antonietti, M. Oschatz, "Giant" nitrogen uptake in ionic liquids confined in carbon pores. *J. Am. Chem. Soc.* **143**, 9377–9384 (2021).

22. C. N. R. Rao, G. R. Rao, Nature of nitrogen adsorbed on transition metal surfaces as revealed by electron spectroscopy and cognate techniques. *Surf. Sci. Rep.* **13**, 223–263 (1991).

23. M. Kitano *et al.*, Ammonia synthesis using a stable electride as an electron donor and reversible hydrogen store. *Nat. Chem.* **4**, 934–940 (2012).

24. H. Zhong *et al.*, Boosting the electrocatalytic conversion of nitrogen to ammonia on metal-phthalocyanine-based two-dimensional conjugated covalent organic frameworks. *J. Am. Chem. Soc.* **143**, 19992–20000 (2021).

25. H. Zou, W. Rong, S. Wei, Y. Ji, L. Duan, Regulating kinetics and thermodynamics of electrochemical nitrogen reduction with metal single-atom catalysts in a pressurized electrolyser. *Proc. Natl. Acad. Sci. U.S.A.* **117**, 29462–29468 (2020).

26. J. B. Geri, J. P. Shanahan, N. K. Szymczak, Testing the push-pull hypothesis: Lewis acid augmented N_2 activation at iron. *J. Am. Chem. Soc.* **139**, 5952–5956 (2017).

27. Y. Hao *et al.*, Promoting nitrogen electroreduction to ammonia with bismuth nanocrystals and potassium cations in water. *Nat. Catal.* **2**, 448–456 (2019).

28. M. Wang *et al.*, Salting-out effect promoting highly efficient ambient ammonia synthesis. *Nat. Commun.* **12**, 3198 (2021).

29. R. J. Gillespie, T. E. Peel, Hammett acidity function for some superacid systems. II. Systems sulfuric acid-[fsa], potassium fluorosulfate-[fsa], [fsa]-sulfur trioxide, [fsa]-arsenic pentafluoride, [sfa]-antimony pentafluoride and [fsa]-antimony pentafluoride-sulfur trioxide. *J. Am. Chem. Soc.* **1374**, 5173–5178 (1952).

30. K. Kuhlrnannib, D. M. Grant, Spin-spin coupling in the tetrafluoroborate ion. *J. Phys. Chem.* **68**, 3208–3213 (1964).

31. C. A. Wamser, Equilibria in the system boron trifluoride-water at 25°. *J. Am. Chem. Soc.* **73**, 409–416 (1951).

32. L. Han *et al.*, Local modulation of single-atomic mn sites for enhanced ambient ammonia electrosynthesis. *ACS Catal.* **11**, 509–516 (2021).

33. M. Zheng *et al.*, A simple additive-free approach for the synthesis of uniform manganese monoxide nanorods with large specific surface area. *Nanoscale Res. Lett.* **8**, 166 (2013).

34. L. Zhang *et al.*, Boosting electrocatalytic N_2 reduction by MnO_2 with oxygen vacancies. *Chem. Commun. (Camb.)* **55**, 4627–4630 (2019).

35. M. Wang *et al.*, Over 56.55% Faradaic efficiency of ambient ammonia synthesis enabled by positively shifting the reaction potential. *Nat. Commun.* **10**, 341 (2019).

36. L. Shi, Y. Yin, S. Wang, H. Sun, Rational catalyst design for n 2 reduction under ambient conditions: Strategies toward enhanced conversion efficiency. *ACS Catal.* **10**, 6870–6899 (2020).

37. X. Liu, Y. Jiao, Y. Zheng, M. Jaroniec, S. Z. Qiao, Building up a picture of the electrocatalytic nitrogen reduction activity of transition metal single-atom catalysts. *J. Am. Chem. Soc.* **141**, 9664–9672 (2019).

38. A. Biswas *et al.*, Alteration of electronic band structure *via* a metal-semiconductor interfacial effect enables high Faradaic efficiency for electrochemical nitrogen fixation. *ACS Nano* **15**, 20364–20376 (2021).

39. U. K. Ghorai *et al.*, Scalable production of cobalt phthalocyanine nanotubes: Efficient and robust hollow. *ACS Nano* **15**, 5230–5239 (2021).

40. S. Murmu *et al.*, Unveiling the genesis of the high catalytic activity in nickel phthalocyanine for electrochemical ammonia synthesis. *J. Mater. Chem. A Mater. Energy Sustain.* **9**, 14477–14484 (2021).

41. C. He *et al.*, Identification of FeN_4 as an efficient active site for electrochemical N_2 reduction. *ACS Catal.* **9**, 7311–7317 (2019).

42. B. Hammer, J. K. Norskov, Why gold is the noblest of all the metals. *Nature* **376**, 238–240 (1995).

43. F. Lai *et al.*, N_2 electroreduction to NH_3 by selenium vacancy-rich $ReSe_2$ catalysis at an abrupt interface. *Angew. Chem. Int. Ed. Engl.* **59**, 13320–13327 (2020).

44. X. Guo *et al.*, Tackling the activity and selectivity challenges of electrocatalysts toward the nitrogen reduction reaction via atomically dispersed biatom catalysts. *J. Am. Chem. Soc.* **142**, 5709–5721 (2020).

45. W. Qiu *et al.*, High-performance artificial nitrogen fixation at ambient conditions using a metal-free electrocatalyst. *Nat. Commun.* **9**, 3485 (2018).

46. C. Choi *et al.*, Suppression of hydrogen evolution reaction in electrochemical N2 reduction using single-atom catalysts: A computational guideline. *ACS Catal.* **8**, 7517–7525 (2018).

47. S. Wu *et al.*, Removal of hydrogen poisoning by electrostatically polar MgO support for low-pressure NH_3 synthesis at a high rate over the Ru catalyst. *ACS Catal.* **10**, 5614–5622 (2020).

48. T. Wang, F. Abild-Pedersen, Achieving industrial ammonia synthesis rates at near-ambient conditions through modified scaling relations on a confined dual site. *Proc. Natl. Acad. Sci. U.S.A.* **118**, e2106527118 (2021).